Marine and Petroleum Geology 48 (2013) 8–19

Contents lists available at ScienceDirect

Marine and Petroleum Geology

journal homepage: www.elsevier.com/locate/marpetgeo

A preliminary study on the pore characterization of Lower Silurian black shales in the Chuandong Thrust Fold Belt, southwestern China using low pressure N_2 adsorption and FE-SEM methods

Hui Tian [a], Lei Pan [a], Xianming Xiao [a,*], Ronald W.T. Wilkins [b], Zhaoping Meng [c], Baojia Huang [d]

[a] State Key Laboratory of Organic Geochemistry, Guangzhou Institute of Geochemistry, Chinese Academy of Sciences, Guangzhou 510640, China
[b] CSIRO Earth Science and Resource Engineering, P.O. Box 136, North Ryde, NSW, Australia
[c] College of Geoscience and Surveying Engineering, China University of Mining & Technology (Beijing), Beijing 100083, China
[d] CNOOC Ltd, Zhanjiang 524057, China

ARTICLE INFO

Article history:
Received 20 May 2013
Received in revised form
11 July 2013
Accepted 13 July 2013
Available online 20 July 2013

Keywords:
Shale gas
Pore structure
Lower Silurian shale
Sichuan Basin

ABSTRACT

Although Lower Silurian black shales within and around the Sichuan Basin have received renewed attention during the past few years because of their potential prospectivity for shale gas, studies associated with shale gas reservoir evaluation are still rare. In this study, eight black shale core samples were collected from a well drilled recently in the Chuandong Thrust Fold Belt, southwestern China, and their geochemistry and pore structures were investigated using low pressure N_2 adsorption analysis and field emission scanning electron microscopy (FE-SEM) observations. The results show that the black shales have total organic carbon (TOC) values ranging from 1.01% to 3.98% and their equivalent vitrinite reflectance values are in the range of 2.84%–3.05%. Both mineral matrix and organic matter pores are well developed with pore sizes ranging from several to several hundred nanometers. The total porosity for the eight samples ranges from 2.60% to 4.74% and the percentages of organic matter pores are estimated to be in the range of 31%–62%. The total surface area ranges from 5.06 m^2/g to 19.32 m^2/g and the micropore (<2 nm) surface area estimated by the t-plot method ranges from 3.13 m^2/g to 9.27 m^2/g. The TOC values have positive relationships with the total porosity, total surface area and the micropore (<2 nm) volume and surface area, indicating TOC may be an effective parameter for shale gas reservoir evaluation in the studied area.

1. Introduction

Organic-rich shales (including mudrocks) have previously been considered as source rocks and seals in a conventional petroleum system for many years (Hunt, 1996). The commercial production of shale gas and shale oil, however, has changed this idea and the mudrocks have received renewed attention in recent years because of their emergence as effective hydrocarbon reservoirs (Curtis, 2002; Montgomery et al., 2005; Jarvie et al., 2007; Pollastro, 2007; Loucks et al., 2009). A shale gas system is an unconventional petroleum system in which the shale acts as both the source of, and the reservoir for, hydrocarbon gases that are derived from the organic matter within the shales through biogenic and/or thermogenic processes (Krooss et al., 1995; Hill et al., 2007; Strąpoć et al., 2010). Shale gas is stored in one or more of three forms: (1) free gas in pores and fractures, (2) adsorbed gas in organic matter and on inorganic minerals, and (3) dissolved gas in oil and water (Curtis, 2002; Zhang et al., 2012). The identification of porosity and pore size distribution in gas shales has become a high research priority as they are key parameters for the commercial evaluation of a potential shale (Ross and Bustin, 2008, 2009; Loucks et al., 2009). Compared with micrometer scale pores in sandstone and carbonate reservoirs, the pores within shale gas reservoirs are usually smaller than one micrometer in size. Especially the pores hosted in organic grains have sizes in the range of several to several hundreds of nanometers (Chalmers et al., 2009, 2012a, b; Loucks et al., 2009; Nelson, 2009; Milliken et al., 2013). Thus Chalmers et al. (2009) recommended that geoscientists working on shales

* Corresponding author. State Key Laboratory of Organic Geochemistry, Guangzhou Institute of Geochemistry, Chinese Academy of Sciences, 511#, Kehua Road, Tianhe District, Guangzhou City 510640, Guangdong Province, China. Tel.: +86 2085290176; fax: +86 2085290706.
E-mail address: xmxiao@gig.ac.cn (X. Xiao).

0264-8172/$ – see front matter © 2013 Elsevier Ltd. All rights reserved.
http://dx.doi.org/10.1016/j.marpetgeo.2013.07.008

use the pore size terminology of the International Union of Pure and Applied Chemistry, with micropores having widths less than 2 nm, mesopores between 2 and 50 nm, and macropores greater than 50 nm.

To elucidate the complex pore systems of shales, researchers have utilized several measurement techniques to characterize the porosity, specific surface area and pore size distribution. Typically the total porosity of shale is calculated by the difference between grain density and bulk density measured by He pycnometry and Hg immersion, respectively (Chalmers et al., 2012a,b), while the surface area and pore size distribution can be obtained by low pressure N_2 and CO_2 gas adsorption, mercury injection capillary pressure (MICP) (Chalmers and Bustin, 2007a,b; Ross and Bustin, 2009; Mastalerz et al., 2012; Kuila and Prasad, 2013; Schmitt et al., 2013) and small angle and ultra small angle neutron scattering techniques (SANS/USANS) (Clarkson et al., 2012a; Mastalerz et al., 2012). Field emission scanning electron microscopy/transmission electron microscopy (FE-SEM/TEM) and focused ion beam scanning electron microscopy (FIB-SEM) have also been successfully used to observe the shapes, sizes and distributions of pores in shales (Loucks et al., 2009; Bernard et al., 2012; Chalmers et al., 2012a; Milliken et al., 2013).

Compared with the extensive investigations into shale gas reservoirs in North America, similar studies in China have only received attention in recent years (e.g. Wang et al., 2009; Zou et al., 2010). In China three sets of marine shales have developed in southern China, including the Lower Cambrian, Upper Ordovician to Lower Silurian and Upper Permian shales (Zou et al., 2010). Among them, the Lower Cambrian and Upper Ordovician to Lower Silurian shales within and around Sichuan Basin are believed to be the primary gas shale targets because of their widespread occurrence, high content of organic matter, favorable mineral composition and large thickness as indicated from analysis of many outcrops and a few core samples (Wang et al., 2009; Zou et al., 2010; Chen et al., 2011; Huang et al., 2012; Liang et al., 2012; Long et al., 2012; Sun et al., 2012). In this study, eight black shale core samples from the Lower Silurian Longmaxi Formation in the Chuandong Thrust Fold Belt were preliminarily investigated for pore characterization, including total porosity, surface area, pore type and pore size distribution. These data could be used for the further OGIP (original gas in place) evaluation of the Longmaxi shales in this region.

2. Geological settings

The Sichuan Basin today is a remnant of the originally much larger Upper Yangtze cratonic sedimentary basin, as part of which, the Chuandong Thrust Fold Belt is resulted from the collisions since Late Triassic times (Fig. 1; Zeng et al., 2012). The Lower Silurian Longmaxi Formation has been recognized as an effective source rock within and around the Sichuan Basin (Zou et al., 2010; Zeng et al., 2012). The Longmaxi Formation consists of a lower section of black shales and silty shales in which graptolite fossils are abundant (Liang et al., 2012). Its middle and upper sections are dominated by greyish-green shales and sandy shales (Fig. 2), indicating variation of depositional environment from deep shelf to shallow shelf (Liang et al., 2012). The thickness of the black shales varies from several tens of meters to more than one hundred meters with depositional centers in the southern and eastern parts of the Sichuan Basin as well as the Chuandong Thrust Fold Belt, but they are absent in the western-central part of the Sichuan Basin (Fig. 1). The total organic carbon contents of the black shales are lower in the southwestern areas of the Sichuan Basin, ranging from 0.5% to 1.0%, but are higher in the eastern part of the basin and in the Chuandong Thrust Fold Belt, ranging from 1.0% to 4.0% (Fig. 1).

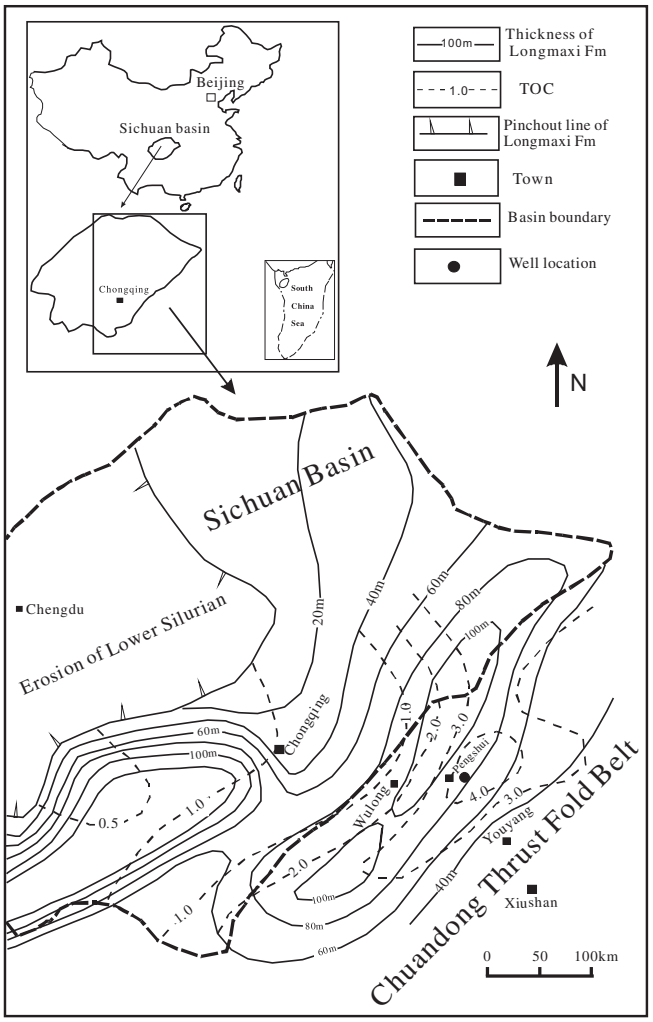

Figure 1. Contour map and TOC distribution of the Lower Silurian Longmaxi Fm black shales within and around the Sichuan Basin (simplified from Zeng et al., 2012). Note that both the Sichuan Basin today and the Chuandong Thrust Fold Belt are parts of originally much larger Upper Yangtze cratonic sedimentary basin (Zeng et al., 2012).

Kerogen types of the organic matter in the black shales of the Longmaxi Formation are dominated by Types I and II with equivalent vitrinite reflectance values in the range of 2.0%–3.0%, indicating their promising prospectivity for shale gas (Zou et al., 2010). Exploration activities within and around the Sichuan Basin have been initiated by many companies, including Petrochina, Chevron, Shell, EOG Resources, Newfield Exploration, and ConocoPhillips (U.S. Energy Information Administration (EIA), 2011). Recently, Sinopec has also entered this area and has drilled several wells in the Chuandong Thrust Fold Belt (Fig. 1), with encouraging gas shows in the Longmaxi black shales encountered for some of the wells, indicating promising potential of shale gas in this region (Ma et al., 2012).

3. Samples and methods

3.1. Samples

One of the wells designed for the evaluation of the Longmaxi Formation shales was drilled recently in the Pengshui County in the Chuandong Thrust Fold Belt (Fig. 1). Eight core samples of the shales were collected from the well in the interval 2122–2150 m (Table 1). The shale samples are black in color with visible graptolite fossils,

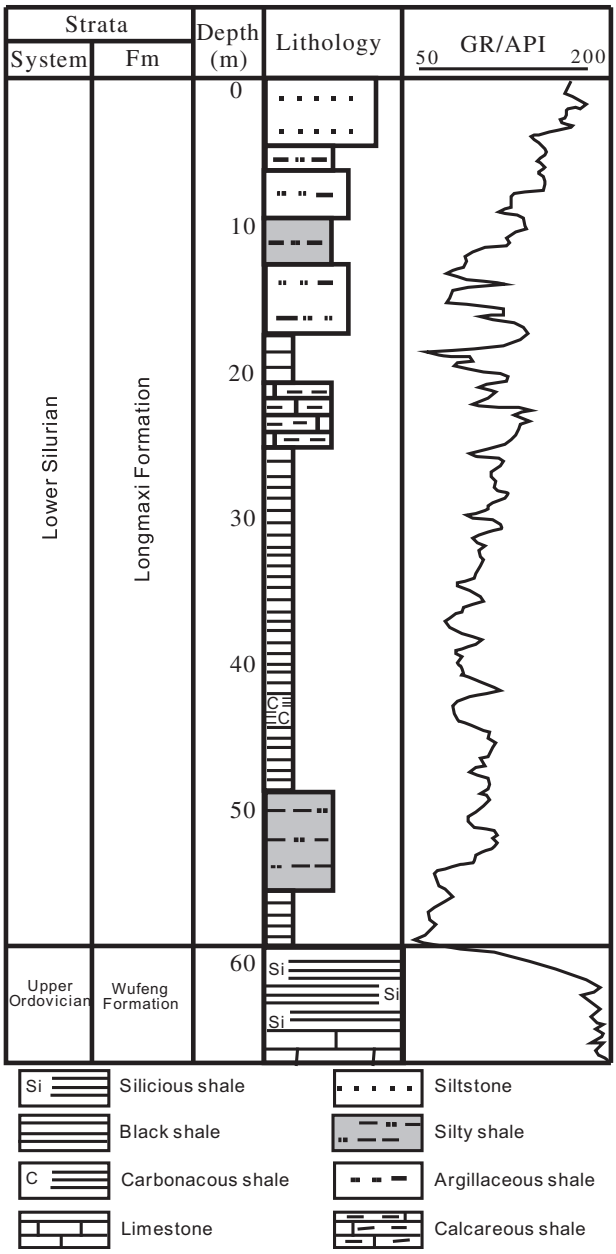

Figure 2. Generalized lithological variations of the Lower Silurian Longmaxi Fm in the Chuandong Thrust Fold Belt (Liang et al., 2012). The samples used in this study located within the interval of 20–50 m.

indicating they were deposited in an anoxic to suboxic environment.

3.2. Organic geochemistry and petrology

The total organic carbon (TOC) was measured by LECO CS-200 analyzer after the samples were treated by hydrochloric acid to remove the carbonates.

Due to the lack of vitrinite in the sampled shales, pyrobitumen reflectance measurements were carried out on polished blocks under reflected light using a 3Y microphotometric system. The percent random reflectance was measured in oil immersion ($n = 1.518$) at 546 nm using a 50 × /0.85 objective lens. The pyrobitumen reflectance (BRr) was then converted to equivalent vitrinite reflectance (VRr) using the equation of Schoenherr et al. (2007), i.e., $VRr = (BRr + 0.2443)/1.0495$.

X-ray diffraction (XRD) analysis of shale powders was carried out on a Bruker D8 Advance x-ray diffractometers at 40 kV and 30 mA with a Cu Kα radiation ($\lambda = 1.5406$ for CuKα1). Stepwise scanning measurements were performed at a rate of 4°/min in the range of 3°–85° (2θ). The relative mineral percentages were estimated semi-quantitatively using the area under the curve for the major peaks of each mineral with correction for Lorentz Polarization (Chalmers and Bustin, 2008).

3.3. Determination of total porosity

As illustrated by Chalmers et al. (2012a), the total porosity of shales can be determined by bulk density (ρ_{bulk}) coupled with skeletal density ($\rho_{skeletal}$). Samples (40–50 g) crushed between 20 and 40 mesh sizes (830 and 380 μm) and dried at 110 °C were used in determining the skeletal density by helium pycnometry at a pressure of less than 25 psia. For the bulk density, the samples were first weighted in the air (M^{air}_{sample}), then they were sealed by paraffin with known density ($\rho_{paraffin}$) and weighted again in the air ($M^{air}_{sample\ +\ paraffin}$) and water ($M^{water}_{sample\ +\ paraffin}$), respectively. The density of water (ρ_{water}) was measured to be 0.9975 cm^3/g at room temperature. Thus the mixed volume of sample and paraffin ($V_{sample\ +\ paraffin}$) was determined by Equation (1):

$$V_{sample+paraffin} = \frac{M^{air}_{sample+paraffin} - M^{water}_{sample+paraffin}}{\rho_{water}} \quad (1)$$

The bulk volume and density of samples (V_{sample} and ρ_{bulk}) was respectively determined by Equations (2) and (3):

$$V_{sample} = V_{sample+paraffin} - \frac{M^{air}_{sample+paraffin} - M^{air}_{sample}}{\rho_{paraffin}} \quad (2)$$

Table 1
TOC, pyrobitumen bitumen reflectance and mineralogical composition.

Samples	Depth (m)	TOC (%)	Pyrobitumen reflectance (%)	Relative percent (%)							
				Quartz	Feldspar	Carbonate	Total clays[a]	Illite	Montmorillonite	Chlorite	Pyrite
Sample1	2122.5	1.42	nd[b]	22.7	29.3	2.8	45.1	20.1	8.2	16.8	nd
Sample2	2126.8	1.01	nd	24.9	17.6	10.3	44.9	28.0	9.0	7.9	2.2
Sample3	2131.3	1.56	2.77	21.6	27.3	3.6	44.3	20.5	10.1	13.7	3.2
Sample4	2134.5	1.30	2.83	28.7	16.0	10.0	44.1	20.5	10.8	12.8	1.2
Sample5	2136.8	2.62	2.74	27.0	17.4	13.3	38.5	19.4	9.6	9.5	3.9
Sample6	2140.8	3.47	nd	29.3	8.0	10.2	52.5	26.2	16.9	9.4	nd
Sample7	2144.8	3.41	2.96	30.5	10.2	6.30	49.2	20.8	18.8	9.6	3.8
Sample8	2149.7	3.98	2.84	30.1	10.6	5.2	52.5	33.0	17.4	2.1	1.5

[a] Total clays = illite + montmorillonite + chlorite.
[b] No data.

$$\rho_{bulk} = \frac{M^{air}_{sample}}{V_{sample}} \quad (3)$$

Then the total porosity was calculated from the difference between the bulk and skeletal densities using Equation (4):

$$\phi = 100 \times \left(1 - \frac{\rho_{bulk}}{\rho_{skeletal}}\right) \quad (4)$$

3.4. Low pressure nitrogen gas adsorption

Low pressure nitrogen adsorption isotherms were obtained at −195.8 °C on an accelerated surface area and porosimetry system (ASAP 2020^M, Micromeritics Instruments). The samples were crushed into grains of 60–80 mesh size (250–180 μm), dried in oven at 110 °C overnight and degassed under high vacuum (<10 mmHg) for 12 h at 110 °C in the apparatus. The saturation vapor pressure (p_o) of N_2 at −195.8 °C was determined every 120 min during the experiment using a nitrogen vapor pressure thermometer. The relative pressure (p/p_o) ranges from 0.011 to 0.995 and an equilibration time of 10 s was applied during the analysis. Both adsorption and desorption isotherms were measured to investigate the hysteresis types. The isotherm obtained from N_2 adsorption, when applied over a wide range of relative pressures (p/p_o), can provide information on the surface area, pore volume and pore size distribution (Kuila and Prasad, 2013).

The calculation of specific surface areas (S_{BET}) were based on the BET equation in its linearised from,

$$\frac{p/p_o}{V_{ads}(1 - p/p_o)} = \frac{1}{V_m \cdot C_{BET}} + \frac{C_{BET} - 1}{V_m \cdot C_{BET}} \times \frac{p}{p_o} \quad (5)$$

with p/p_o the relative pressure; V_{ads} the adsorbed volume; V_m the monolayer volume and the constant C_{BET}. To reduce any subjectivity in the assessment of the fitting range of the BET plot and give an objective way of determining the fitting range of the BET plot rather than using the same relative pressure range for all materials, Rouquerol et al. (2007) suggested some criteria for the selection of relative pressure range, including (1) the resulting parameter C_{BET} is positive; (2) the intercept on the ordinate of the BET-plot is positive and (3) the term $V_{ads}(p_o - p)$ should continuously increase with p/p_o, if not, the pressure rang should be narrowed. Then S_{BET} with unit of m^2/g was calculated using the following equation (Sing et al., 1985):

$$S_{BET} = \frac{0.001 \times V_m}{22.4} \times N \times A_{N_2} \quad (6)$$

with V_m the monolayer volume in cm^3/g; N the Avogadro' number; A_{N_2} the atomic surface area of N_2 (0.162 nm^2 at 77 K).

The micropore surface area and volume were estimated using the t-plot method based on the N_2 adsorption (de Boer et al., 1963; Webb and Orr, 1997; Hodson, 1999; Scherdel et al., 2010). In t-plots, the adsorbed N_2 volume (V_{ads}) is plotted against the statistical thickness (t) of the adsorbed layer of N_2 adsorption. If the plot yields a straight line that passes through the origin, then the sample is considered to be free of micropores. On the contrary, the t-plot of the material containing micropores shows a straight line at medium t values and a concave–down curve at lower t values. At higher t values, convex-up deviation from the linear trend indicates capillary condensation in mesopores. Thus the slope (k) and intercept (b) of the regressed straight line gives the external surface area (S_{ext}, including the surface area from mesopores, macropores and other external surface area) and the micropore volume (V_{mic}), respectively (de Boer et al., 1963). When the V_{ads} is in unit of cm^3/g and t is in unit of angstrom, S_{ext} in unit of m^2/g is given by:

$$S_{ext} = 15.47 \times k \quad (7)$$

and V_{mic} in cm^3/g is given by

$$V_{mic} = 0.001547 \times b \quad (8)$$

Thus the surface area of micropores (S_{mic}) can be estimated by subtracting the external surface area (S_{ext}) calculated by the t-plot method from the total surface area (S_{BET}) obtained by the BET equation (Rouquerol et al., 2007; Webb and Orr, 1997; Hodson, 1999; Scherdel et al., 2010; Kuila and Prasad, 2013).

The most frequently used 'universal thickness curve' is based on the Harkins–Jura model for N_2 adsorption (de Boer et al., 1963):

$$t = \left[\frac{13.99}{0.034 - \log(p/p_o)}\right]^{1/2} \quad (9)$$

Considering the shale samples contain organic matter, the Carbon Black model (Magee, 1995) is also used to calculate the statistical thickness (t):

$$t = 0.88 \times (p/p_o)^2 + 6.45 \times (p/p_o) + 2.98 \quad (10)$$

Where, p/p_o is the relative pressure and the unit of t is angstrom.

The pore size distribution was calculated using the BJH model that describes the capillary condensation phenomenon in a cylindrical pore (Barret et al., 1951). It is assumed that the condensation of N_2 in a pore of radius r takes place in the 'core' region, i.e., the inner part of the pore that is calculated by subtracting the statistical thickness (t) from the pore radius r. Using this model, it is predicted that the condensation of nitrogen in a pore of radius r occurs at a pressure given by the following modified Kelvin equation:

$$\ln(p/p_o) = -\frac{\alpha \gamma_N V_1}{RT(r - t)} \quad (11)$$

Where, p/p_o is the relative pressure, γ_N and V_1 are the surface tension and molar volume of liquid nitrogen, respectively; R is the gas constant, T is the temperature at which the isotherm is measured and α is a factor that accounts for the shape of the gas/liquid interface. During the adsorption process, the shape is assumed to be cylindrical and the value of α is 1 (Coasne et al., 2004). The statistical thickness (t) was calculated by the Harkins–Jura model for N_2 adsorption (de Boer et al., 1963).

3.5. FE-SEM observation

The FE-SEM imaging of nanopores was performed on the surfaces prepared by Ar ion milling (IM4000, Hitachi High-Tech) using an accelerating voltage of 3 kV and a milling time of 4 h. Secondary electron (SE) images for documenting topographic variation and BSE images for delineating compositional variation were acquired on both the Hitachi S4800 and the FEI Helios NanoLab™ 600 systems. These images provided important qualitative information on general locations of pores throughout the sample (Loucks et al., 2009). Lower accelerating voltages (1–5 kV) with working distances of 1.5–8 mm were typically used on these systems to prevent beam damage of the samples.

4. Results and discussions

4.1. Organic geochemistry and petrology

The total organic carbon contents (TOC) for the eight core shale samples range from 1.01% to 3.98% (Table 1). The organic fraction is dominated by maceral assemblages of micrinite, interpreted as the

residual organic matter after oil generation and expulsion (Stach et al., 1982; Ross and Bustin, 2009), and pyrobitumen formed by the cracking of retained oil in shales (Pepper and Dodd, 1995; Bernard et al., 2012; Mahlstedt and Horsfield, 2012). The measured pyrobitumen reflectance values range between 2.74% and 2.96% (Table 1) and the equivalent vitrinite reflectances using the equation of Schoenherr et al. (2007) are in the range of 2.84–3.05%, within the dry gas generation window. The mineralogical compositions of the eight black shale samples are listed in Table 1 and summarized in a tertiary diagram (Fig. 3). All the samples are clay rich, ranging from 38% to 53%, and no apparent trend between TOC values and the total clay contents was observed. The carbonate contents vary from 2.8% to 13.3%, whereas the feldspar contents range from 8.0% to 29.3%. The quartz contents vary from 21.6% to 30.5% and show a weak positive relationship with TOC (Fig. 4). As illustrated by Chalmers et al. (2012b), the positive relationship between quartz and TOC contents is due to the biogenic origins of quartz. Compared with the Devonian gas shales in Horn River Basin, Canada (Chalmers et al., 2012b), our samples contain less quartz of biogenic origins.

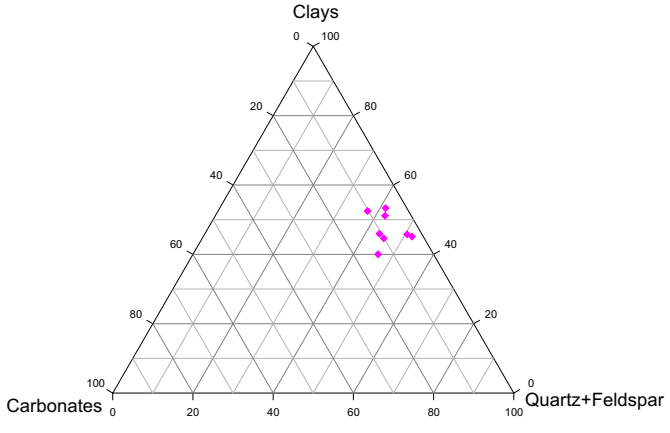

Figure 3. Ternary diagram of the mineralogical compositions of the black shales from the Longmaxi Formation based on the normalized data from Table 1.

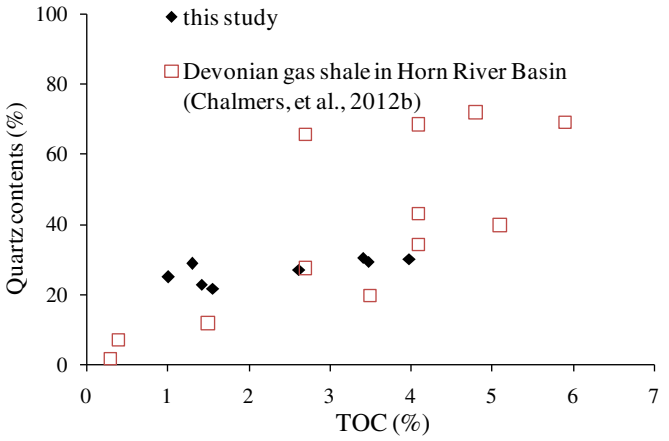

Figure 4. The interrelationship between TOC content and quartz content. The weakly positive relationship indicates the quartz of biogenic origin is minor for our samples. The reference data are from Devonian gas shales in the Horn River Basin, northeastern British Columbia, Canada (Chalmers et al., 2012b).

4.2. Pore types and total porosity

Loucks et al. (2012) presented a comprehensive investigation into the pores within gas shales and grouped them to three types: (1) mineral matrix pores between or within mineral particles; (2) pores within organic matter and (3) fracture pores that are not controlled by individual particles. Two samples were selected for FE-SEM imaging based on their TOC contents. Figure 4 presents FE-SEM images of pores in Sample 4, which has a lower organic matter content (TOC = 1.3%), to illustrate the pore types. The mineral matrix pores are mainly developed between and within clay minerals and pyrite framboids (Fig. 5a, b). The cracks were also observed (Fig. 5a) and are possibly caused by shrinking of clay minerals and/or decompression effect after the retrieval from subsurface (Chalmers et al., 2012a). The organic matter hosted pores are developed with pore size ranging from several nanometers to more than one hundred nanometers (Fig. 5c, d). These pores may be connected by narrow throats in the 2D image (Fig. 5d), though 3D images are more helpful to confirm this connection. The FE-SEM images of organic matter pores from Sample 8 with a higher organic matter content (TOC = 3.98%) are also presented in Figure 6. Similar to Sample 4, the organic matter pores in Sample 8 are developed in various shapes and sizes, illustrating that the organic-matter pores in studied samples are similarly developed because of their similarities in both organic matter type and thermal maturity level.

Although FE-SEM imaging can provide many qualitative information on the pore types in shales (Loucks et al., 2009; Curtis et al., 2012; Milliken et al., 2013), the total porosity is usually calculated by the difference between the bulk and grain densities (Chalmers et al., 2012a). The total porosity of the eight samples ranges between 2.60% and 4.74% (Table 2) and these values are within the porosity range of the North American shales (Bruner and Smosna, 2011; Chalmers et al., 2012a,b; Hao and Zou, 2013). Except for Sample 4, there is a positive relationship between the total porosity and TOC, with a regressed slope and intercept of 0.719 and 1.783, respectively (Fig. 7a). When the regression line is extrapolated to TOC = 0, a porosity of 1.783% is obtained. We then assume that this value is the total porosity contributed by inorganic pores because the TOC is zero. Of course, the validity of this assumption depends on the dataset and the more data, the more accurate. Thus the pores contributed by the organic matter are estimated in the range of 31.3%–62.6% of the total porosity (Fig. 7b). The significant contribution (over 75%; Loucks et al., 2012) of organic matter pores in gas shales was also reported from the Mississippian Barnett shale of the Fort Worth Basin, Texas, which has a nanopore size ranging from several to several hundreds of nanometers (Loucks et al., 2009, 2012; Chalmers et al., 2012a; Milliken et al., 2013). Sample 4 has a total porosity of up to 4.71%, but its TOC value is only 1.3%, indicating there are more mineral matrix pores than other samples. However, Sample 4 is also beyond the normal trends in the plot of *total porosity vs. total clays* (Fig. 7c), indicating there are other factors that contribute to the porosity. Although we can not provide definite reasons on this abnormity due to our limited dataset, we assume that it is probably the pyrite that contributes to this additional porosity. We also noted that the pyrite content of Sample 4 is not the largest among the samples. However, the porosity from pyrite is mainly related to the pyrite framboids (Loucks et al., 2009). Therefore detailed investigations on the shapes and structures of pyrite should be carried out in the future.

4.3. Isotherms of N_2 adsorption and desorption

The isotherms of adsorption and desorption of N_2 at liquid nitrogen temperature (−195.8 °C) are presented in Figure 8. The adsorption amount at p/p_o around 0.995 varies from 9.2 cm^3/g to 17.0 cm^3/g for different samples, and shows a positive relationship

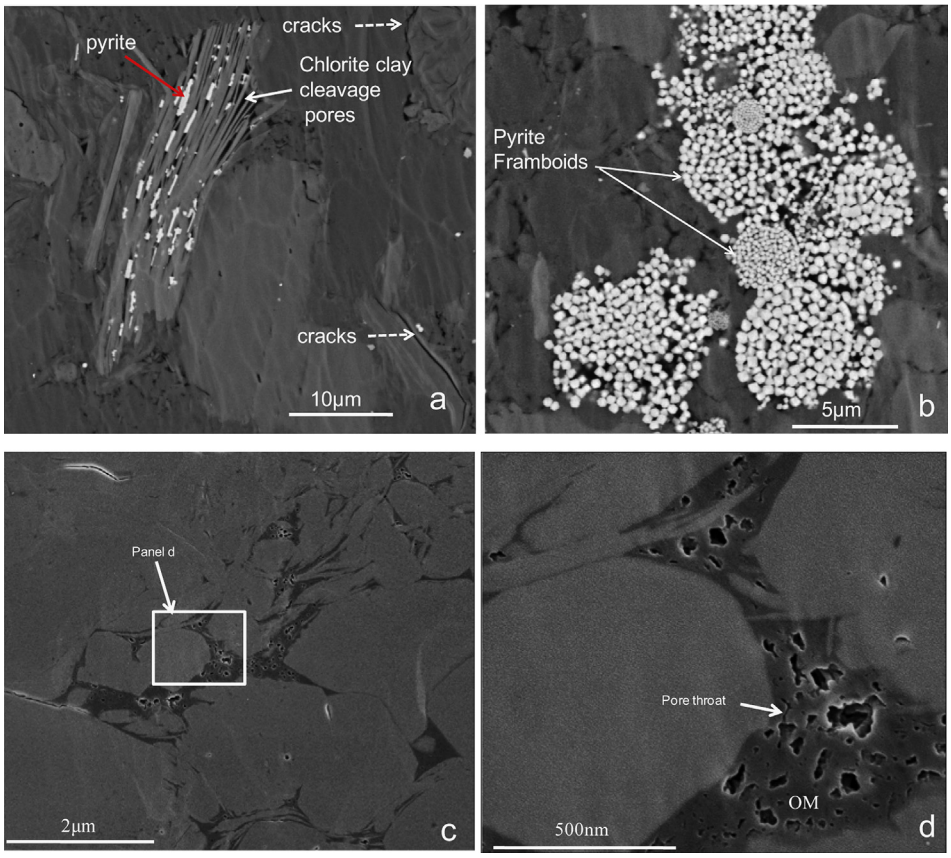

Figure 5. Field emission scanning electron microscope (FE-SEM) images of a black shale from the Longmaxi Formation (TOC = 1.30%, Sample 4) showing the mineral matrix pores and cracks (a, b) and organic matter pores (c, d). OM = organic matter.

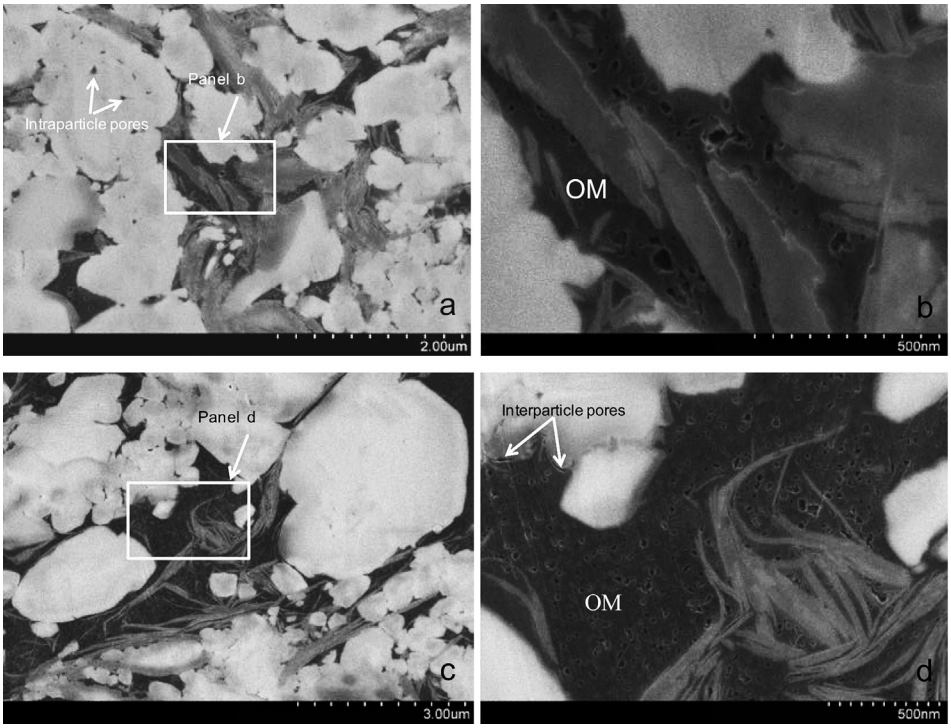

Figure 6. Field emission scanning electron microscope (FE-SEM) images of the organic-matter pores in Sample 8 of the Longmaxi Fm black shales (TOC = 3.98%). OM = organic matter.

Table 2
Grain density, bulk density, total porosity, total surface area, and the external surface area and micropore volume based on t-plot method (see details in Method section).

Samples	Depth (m)	Grain density (cm^3/g)	Bulk density (cm^3/g)	Total porosity (%)	S_{BET} (m^2/g)	t-plot method[a]					
						Harkins–Jura model (de Boer et al., 1963)			Carbon Black model (Magee, 1995)		
						S_{ext} (m^2/g)	S_{mic} (m^2/g)	V_{mic} ($m^3/100$ g)	S_{ext} (m^2/g)	S_{mic} (m^2/g)	V_{mic} ($m^3/100$ g)
Sample1	2122.5	2.6571	2.5762	3.04	9.31	4.36	4.95	0.224	5.04	4.27	0.183
Sample2	2126.8	2.6739	2.6001	2.76	5.06	3.01	2.05	0.088	3.13	1.93	0.082
Sample3	2131.3	2.6486	2.5798	2.60	7.86	3.97	3.89	0.175	4.46	3.40	0.145
Sample4	2134.5	2.7884	2.6570	4.71	6.11	3.54	2.57	0.110	3.66	2.45	0.105
Sample5	2136.8	2.6390	2.5562	3.14	12.94	2.75	10.19	0.433	3.22	9.72	0.405
Sample6	2140.8	2.6289	2.5037	4.76	16.51	6.54	9.97	0.448	7.76	8.75	0.374
Sample7	2144.8	2.6094	2.5047	4.01	15.91	6.74	9.17	0.467	7.94	7.97	0.393
Sample8	2149.7	2.5951	2.4721	4.74	19.32	7.81	11.51	0.519	9.27	10.05	0.429

[a] The t-plot method uses two models. S_{ext} for surface area of pores other than micropores; S_{mic} for surface area of micropores; V_{mic} for micropore volume.

with TOC. All the isotherms show a hysteresis pattern but do not show a plateau at high p/p_o like the Type IV isotherm (Sing et al., 1985). Such an isotherm shape indicates that the material contains both mesopores and macropores (Sing et al., 1985). All the isotherms exhibit adsorption at low relative pressure ($p/p_o < 0.01$), indicating the presence of micropores. The isotherms also show the 'forced closure' of the desorption branch at $p/p_o \approx 0.45$, which is referred to as the 'Tensile Strength Effect' and is a result of instability of the hemispherical meniscus during desorption in pores with critical diameters approximately 4 nm (Groen et al., 2003).

A close examination of the hysteresis loops for the eight samples reveals that they are Type H3, which is usually associated with aggregates of plate-like particles giving rise to slit-shaped pores (Sing et al., 1985). Nevertheless, for natural materials, such as seal or shale rocks, this interpretation has to be considered with caution since it is subject to error (Schmitt et al., 2013). Such a caution was also echoed by Clarkson et al. (2012a) who studied similar tight gas sandstones using USANS/SANS and gas adsorption analysis, and found that the assumption of slit-shape pores inferred from hysteresis loop shape was not consistent with the SANS scattering results.

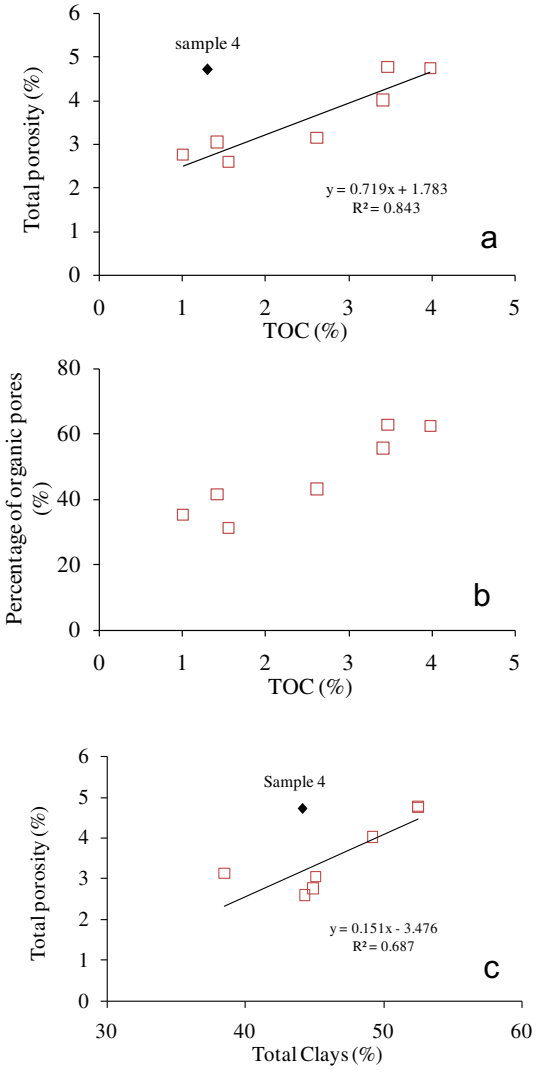

Figure 7. Plots showing the relationships between the total porosity and TOC (a), the percentages of organic-matter pores and TOC (b) and the total porosity and total clays (c) for the shale samples investigated. The porosity contributed by inorganic pores is assumed to be 1.783% by extrapolating TOC value to zero and the porosity of organic-matter pores is calculated by subtracting 1.783% from the total porosity.

4.4. Specific surface area

The specific surface areas calculated from the adsorption isotherms using the BET equation and t-plot method are presented in Table 2. As mentioned previously, the BET method provides the total specific surface area (S_{BET}) while the t-plot method typically provides the external specific surface area (S_{ext}; including mesopores, macropores and other external specific surface area). Therefore the differences in these values can be correlated to the surface area associated with the micropores (Kuila and Prasad, 2013). The total specific surface area (S_{BET}) for the eight samples ranges from 5.06 m^2/g to 19.32 m^2/g and has a positive relationship with TOC (Fig. 9a). This relationship was also previously observed for many gas shale in North American basins (Chalmers and Bustin, 2008; Ross and Bustin, 2009). With the Harkins–Jura model (de Boer et al., 1963), the external surface area (S_{ext}) and micropore surface area (S_{mic}) ranges from 3.01 m^2/g to 7.81 m^2/g and from 2.05 m^2/g to 11.51 m^2/g, respectively. When the Carbon Black model (Magee, 1995) was adopted, these surface areas are a little different, with S_{ext} ranging from 3.13 m^2/g to 9.27 m^2/g and S_{mic} from 1.93 m^2/g to 10.05 m^2/g. Similar to the Devonian–Mississippian Muskwa and Besa River shales from northern British Columbia, western Canada (Ross and Bustin, 2009), the micropore surface areas (S_{mic}) derived by t-plot method show a positive correlation with TOC (Fig. 9b). Note that the S_{ext} also show positive correlation with TOC except for the Sample 5 (TOC = 2.62%) (Fig. 9c), but this abnormal point disappears in the plot of S_{ext} *vs. total clays* (Fig. 9d), which might indicate that it is the low total clays content (38.5%) that results in the low surface areas of meso- and macro-size pores (e.g. S_{ext}). Of course, this interpretation needs to be further confirmed by more samples.

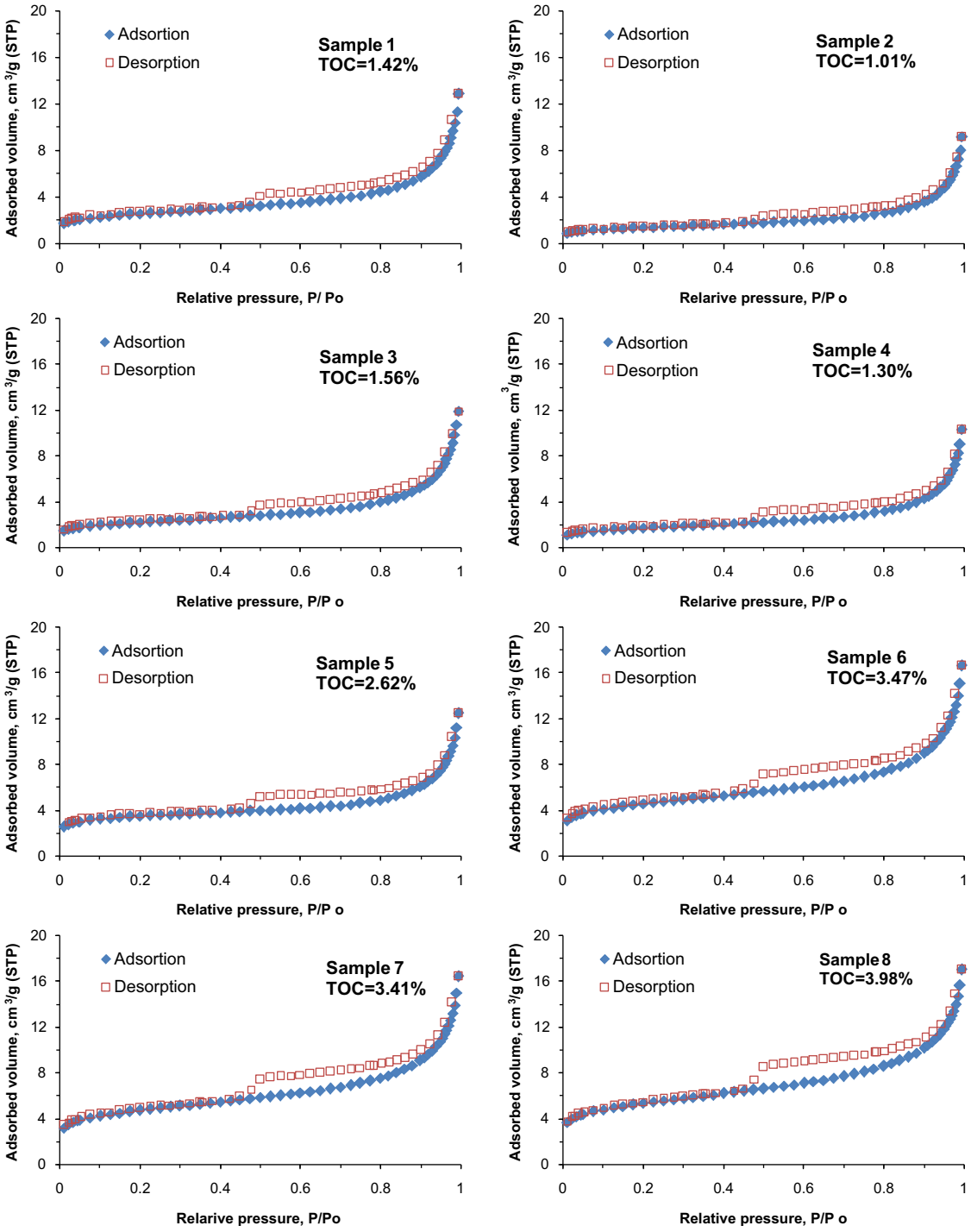

Figure 8. Nitrogen gas adsorption and desorption isotherms for the eight core shale samples at liquid nitrogen gas temperature (−195.8 °C).

4.5. Pore size distribution (PSD)

4.5.1. Plots used for presenting PSD

The distribution of pore volume with respect to pore size can be displayed as cumulative, incremental or differential distribution curves (Meyer and Klobes, 1999; Chalmers et al., 2012a; Clarkson et al., 2012a,b,c; Mastalerz et al., 2012; Kuila and Prasad, 2013). The cumulative curve is a plot of *V* (pore volume) *vs. W* (pore width) from which a differential distribution may be obtained by differentiation. A plot of the derivative of pore volume with respect to pore diameter, i.e., *dV/dW versus W*, is referred to as the differential distribution plot and the pore volume in any pore width range is given by the area under the curve. When the W-axis is logarithmically compressed, the plot of *dV/dlog(W) versus W* is frequently used to display the pore size distribution (Clarkson et al., 2012b,c; Kuila and Prasad, 2013), and more conveniently used to compare the relative pore volumes between any pore size range than the plot of *dV/dW versus W* because the "*visual area*" under the curve of *dV/dlog(W)* is proportional to the real volumes (Fig. 10a). For the evaluation of pore concentrations in any pore size, the plot of *dV/*

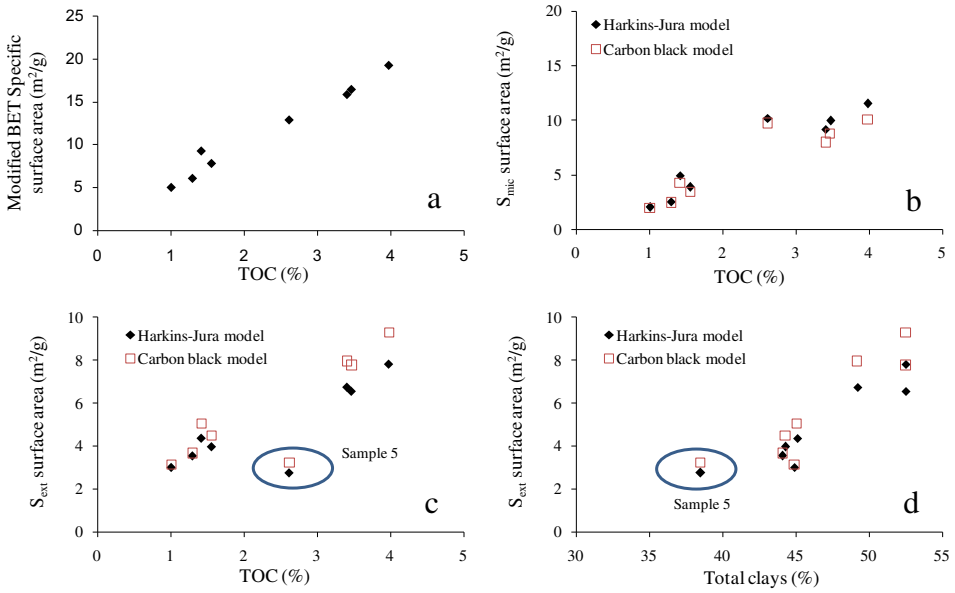

Figure 9. Plots showing the relationships of TOC with total surface area (S_{BET}) (a), micropore surface area (S_{mic}) (<2 nm) (b), external surface area (S_{ext}) (c), and the relationship between total clays content and external surface area (S_{extc}) (d) for the samples analyzed. Note that the abnormally low S_{ext} for Sample 5 with TOC = 2.62% is probably related to its low contents of total clays (38.5%) since the S_{ext} is positively correlated with total clays contents.

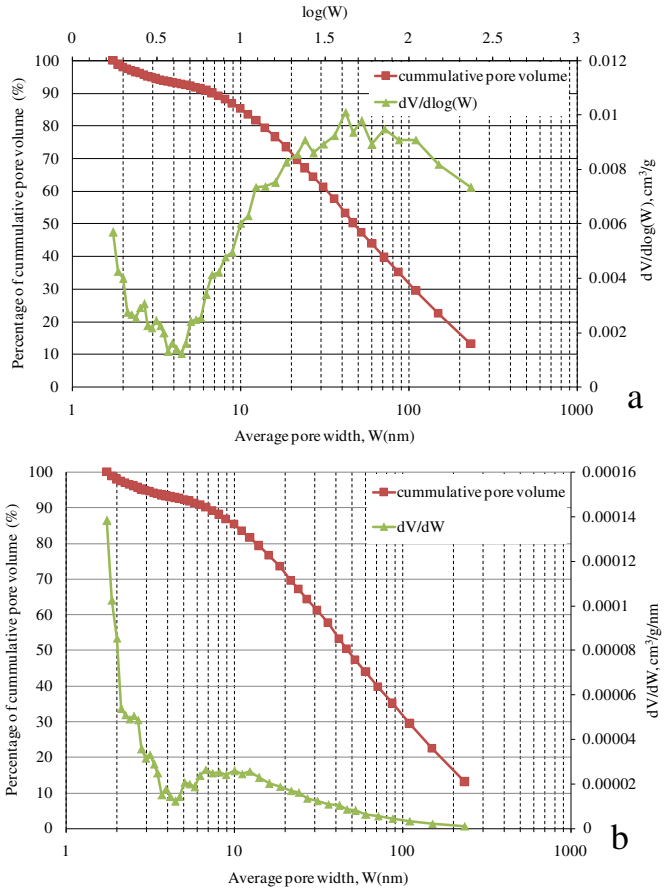

Figure 10. Different presentations of BJH pore size distributions for Sample 5. Note that the plot of *dV/dW versus W* reflects the concentrations of pores of various sizes more accurately than the plot of *dV/dlog(W) versus W*, but the latter can be conveniently applied to investigate the pore volumes over any ranges of pore sizes.

dW versus W (Fig. 10b), however, is better than the plot of *dV/dlog(W) versus W*, and the latter will amplify the concentrations of larger pores because $dV/d\log(W) = 2.303 \times dV/dW \times W$ (Meyer and Klobes, 1999; Clarkson et al., 2012c).

4.5.2. Adsorption vs. desorption branch of isotherms

For the calculation of pore size distribution, the application of the BJH model to the desorption branch of the isotherm that is characterized by a hysteresis loop of type H2 or H3 (Sing et al., 1985) is often much more affected by pore network effects than the adsorption branch. The BJH model will give a completely different result compared to that obtained from the adsorption branch, where the TSE phenomenon is absent (Groen et al., 2003). Figure 11 compares the pore size distributions derived from the adsorption and desorption branch of isotherm for Sample 5. It is clear that the PSD derived from the desorption branch of the isotherm shows a strong artificial pores peak at approximately 4 nm while the selection of the adsorption branch for pore size

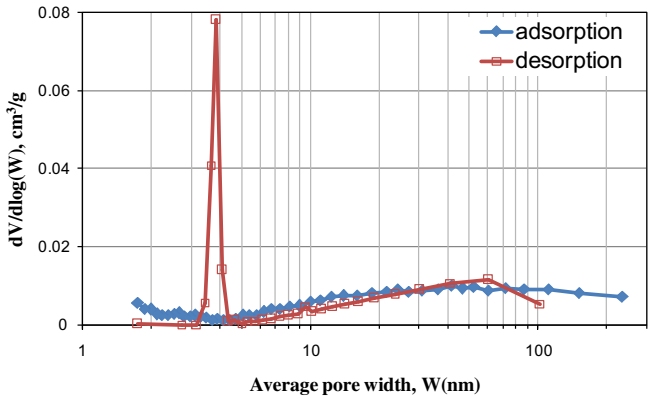

Figure 11. A comparison of BJH pore size distributions derived from the N_2 adsorption and desorption branch of isotherm for Sample 5 to show the artificial peak around 4 nm for desorption branch.

calculations indicates the absence of the well-defined distribution of 4 nm pores, and shows a much broader distribution. Thus when the experimental isotherm shows signs of pore network effects, the adsorption branch is highly preferred for pore size calculations and is hardly affected by the TSE phenomenon (Groen et al., 2003). Since our samples are characterized by an H3 hysteresis loop (Fig. 6), their BJH derived PSDs were calculated using the adsorption branch of isotherm.

4.5.3. Comparison of PSDs for eight samples

As illustrated in Figure 12, the plot of *dV/dW versus W* shows the peak pores have a size of less than 10 nm and the concentrations of pores decrease with the increasing of pore size (Fig. 12a), but the plot of *dV/d(logW) versus W* clearly reveals that it is the larger pores that contribute significantly to the total pore volume (Fig. 12b). This

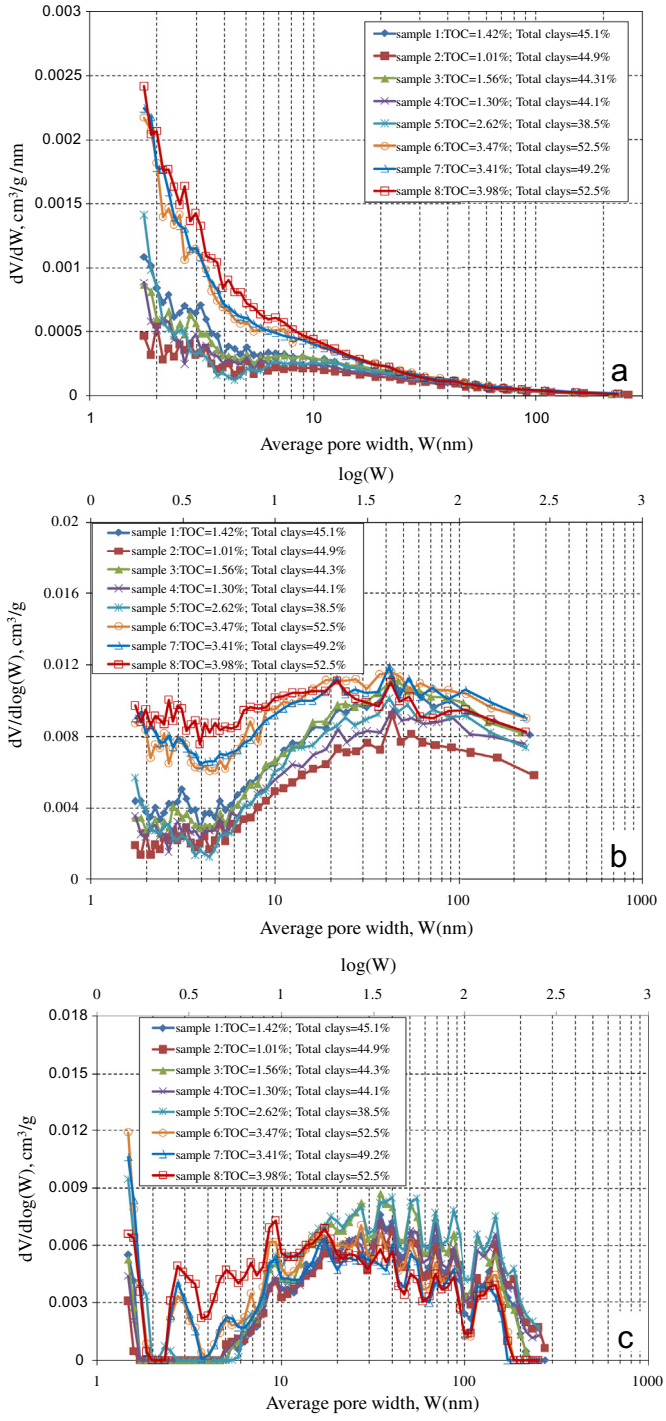

Figure 12. Pore volume distribution with pore size derived from the N_2 adsorption branch for the isotherms of eight core shale samples using BJH model (a, b) and DFT model (c).

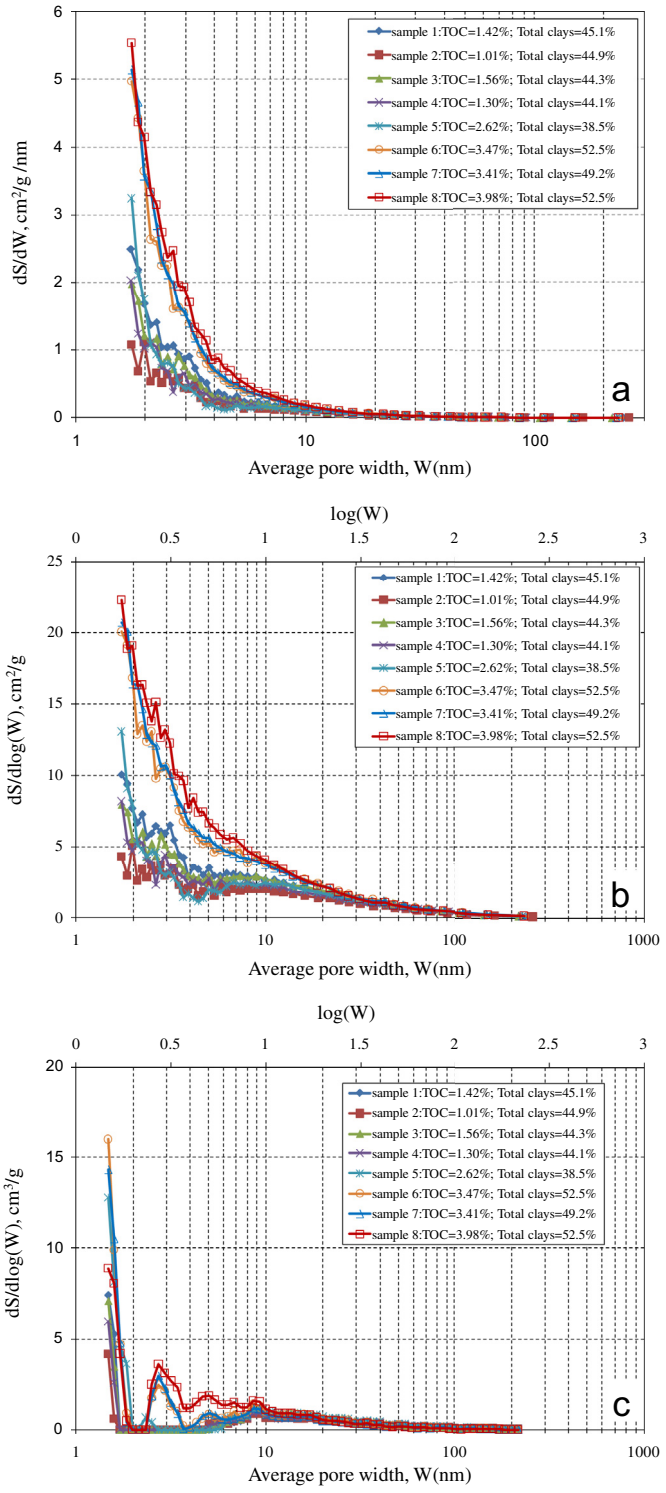

Figure 13. Specific surface area distributions with pore sizes derived from the N_2 adsorption branch of the isotherms of eight core shale samples using BJH model (a, b) and DFT model (c).

is because one large pore can have a volume equal to many small pores. Similar to the PSDs from the BJH model that typically deals with the cylindrical pores, the PSDs calculated by the DFT model developed for carbons with slit-like pores (Dombrowski et al., 2000) also show similar results although the absolute pore volume is somewhat different (Fig. 12c). For the distributions of specific surface area with respect to pore size, the results are presented in Figure 13. While the pore volumes are mainly associated with larger pores (Fig. 12), the specific surface areas are predominantly controlled by smaller pores. Based on the BJH- derived PSDs and the t-plot derived micropore volume and surface areas (Table 2), Figure 14 compares the relative contributions of micropores, mesopores and macropores to the total pore volume and surface area and also reveals that most of the pore volumes are contributed by macropores and mesopores (Fig. 14a), but the surface areas are mainly controlled by micropores and mesopores (Fig. 14b). These observations are consistent with the results for many gas shales in North American basins (Chalmers and Bustin, 2007a,b; Chalmers and Bustin, 2008; Ross and Bustin, 2009). Not that the abnormally low percentage of the mesopores and macropores for Sample 5 with TOC = 2.62% in Figure 14b is probably related to its low contents of total clays (38.5%) because the clays usually provide many mesopore and/or macropore. Meanwhile more fine mesopores (i.e., 2–10 nm) were observed in both the pore volume and specific surface area distributions for Samples 6, 7 and 8 that have higher TOC values than other samples (Figs. 12 and 13), implying that the fine mesopores are more easily developed in organic matter grains than in mineral matrix in the samples analysed.

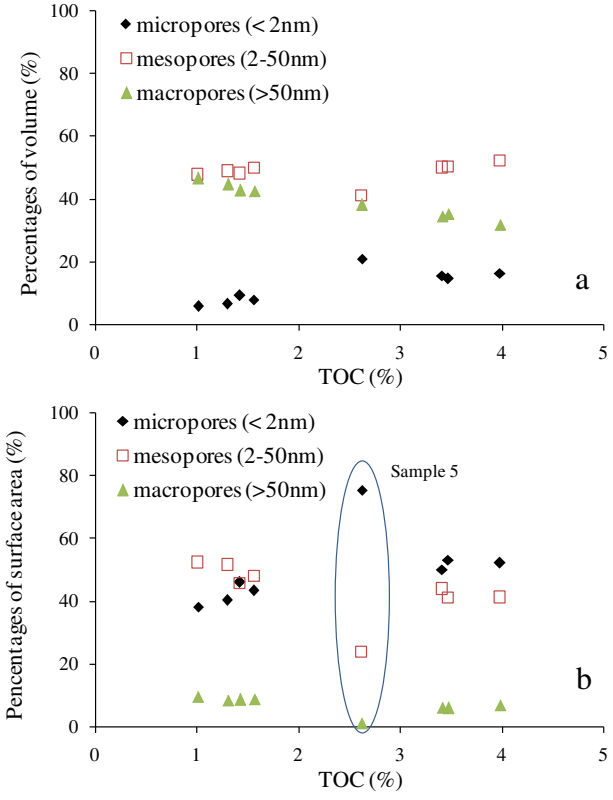

Figure 14. Plots showing relative contributions of micropores, mesopores and macropores to the total pore volume (a) and total surface area (b) based on the results of t-plot method (for micropores) and BJH derived PSD (for meso- and macro-size pores). Note that the abnormally low percentages of meso- and macro-size pore surface areas (e.g. S_{ext}) for Sample 5 with TOC = 2.62% is probably related to its low contents of total clays (See details in Fig. 9d).

5. Conclusions

The pore characteristics of eight black shale samples collected from the Lower Silurian Longmaxi Formation in the Chuandong Thrust Fold Belt were investigated using low pressure N_2 adsorption and FE-SEM observation, with the following preliminary conclusions:

(1) The black shales have moderate contents of organic matter and very high thermal maturities. Their TOC values range from 1.01% to 3.98% and equivalent vitrinite reflectance values are within the range of 2.84%–3.05%. Note that more samples are needed in the future to fully understand the whole set of Lower Silurian Longmaxi black shales.

(2) Similar with shales in North American basins (e.g. Chalmers et al., 2012a,b), both mineral matrix pores and organic matter pores are well developed in the black shales with pore sizes ranging from several to several hundred nanometers. Their total porosity ranges from 2.60% to 4.74% with organic-matter pores in the range of 31%–62% due to their variances in total organic matter contents. The shales have total surface areas (S_{BET}) ranging from 5.06 m^2/g to 19.32 m^2/g and micropore surface areas from 3.13 m^2/g to 9.27 m^2/g.

(3) Both the BJH- and DFT-derived PSDs illustrate that the pore volumes are mainly controlled by larger pores, but the specific surface areas are mainly determined by smaller pores. The total porosity and total surface area, along with the micropore volumes and surface areas derived from t-plot method, have positive relationships with the TOC values, which has been previously shown for many gas shales in North American basins (e.g. Chalmers and Bustin, 2008; Ross and Bustin, 2009). This suggests that TOC could act as an important parameter for shale gas reservoir evaluation in the studied area.

Acknowledgements

The authors are indebted to Profs. Keyu Liu, Gareth R.L. Chalmers and Tongwei Zhang for their insightful scientific comments and language improvements that significantly enhanced the quality of the original manuscript. We are also grateful to Associate Editor Yongtai Yang and Editor-in-Chief O. Catuneanu for their patient editorial work. This study was jointly supported by National Key Basic Research Program of China (973 Program: 2012CB214705), the Tukuangchi Talent Foundation (GIGRC-10-02), and the National Natural Science Fund of China (41072095). Special thanks to FEI Shanghai Labs and Hitachi Beijing Labs for their help with the FE-SEM observations, to Drs Kuila, Marczewski and Prof. Hodson for their instructions on the t-plot method. Hui Tian is also grateful to the Youth Innovation Promotion Association, CAS for financial support. This is contribution No. IS-1718 from GIGCAS.

References

Barret, E.P., Joyner, L.G., Halenda, P.P., 1951. The determination of pore volume and area distribution in porous substances. I. Computations from nitrogen isotherms. Journal of American Chemistry Society 73, 373–380.

Bernard, S., Wirth, R., Schreiber, A., Schulz, H.M., Horsfield, B., 2012. Formation of nanoporous pyrobitumen residues during maturation of the Barnett Shale (Fort Worth Basin). International Journal of Coal Geology 103, 3–11.

Bruner, K.R., Smosna, R., 2011. A Comparative Study of the Mississippian Barnett Shale, Fort Worth Basin, and Devonian Marcellus Shale, Appalachian Basin. DOE/NETL-2011/1478.

Chalmers, G.R., Bustin, R.M., Powers, I., 2009. A pore by any other name would be as small: the importance of meso- and microporosity in shale gas capacity (abs.). AAPG Search and Discovery, 1. Article 90090 http://www.searchanddiscovery.com/abstracts/html/2009/annual/abstracts/chalmers.htm (accessed 14.03.13.).

Chalmers, G.R.L., Bustin, R.M., 2008. Lower Cretaceous gas shales in northeastern British Columbia, part I: geological controls on methane sorption capacity. Bulletin of Canadian Petroleum Geology 56, 1–21.
Chalmers, G.R.L., Bustin, R.M., Power, I.M., 2012a. Characterization of gas shale pore systems by porosimetry, pycnometry, surface area, and field emission scanning electron microscopy/transmission electron microscopy image analyses: examples from the Barnett, Woodford, Haynesville, Marcellus, and Doig units. AAPG Bulletin 96, 1099–1119.
Chalmers, G.R.L., Ross, D.J.K., Bustin, R.M., 2012b. Geological controls on matrix permeability of Devonian Gas Shales in the Horn River and Liard basins, northeastern British Columbia, Canada. International Journal of Coal Geology 103, 120–131.
Chalmers, G.R.L., Bustin, R.M., 2007a. On the effects of petrographic composition on coalbed methane sorption. International Journal of Coal Geology 69, 288–304.
Chalmers, G.R.L., Bustin, R.M., 2007b. The organic matter distribution and methane capacity of the Lower Cretaceous strata of Northeastern British Columbia, Canada. International Journal of Coal Geology 70, 223–339.
Chen, S., Zhu, Y., Wang, H., Liu, H., Wei, W., Fang, J., 2011. Shale gas reservoir characterisation: a typical case in the southern Sichuan Basin of China. Energy 36, 6609–6616.
Clarkson, C.R., Freeman, M., He, L., Agamalian, M., Melnichenko, Y.B., Mastalerz, M., Bustin, R.M., Radlinski, A.P., Blach, T.P., 2012a. Characterization of tight gas reservoir pore structure using USANS/SANS and gas adsorption analysis. Fuel 95, 371–385.
Clarkson, C.R., Jensen, J.L., Pedersen, P.K., Freeman, M., 2012b. Innovative methods for flow-unit and pore-structure analyses in a tight siltstone and shale gas reservoir. American Association of Petroleum Geologists Bulletin 96, 355–374.
Clarkson, C.R., Wood, J.M., Burgis, S.E., Aquino, S.D., Freeman, M., 2012c. Nanopore-structure analysis and permeability predictions for a tight gas siltstone reservoir by use of low pressure adsorption and mercury intrusion techniques. SPE Reservoir Evaluation & Engineering, 641–648.
Coasne, B., Gubbins, K.E., Pellenq, R.J.-M., 2004. A Grand Canonical Monte Carlo study of adsorption and capillary phenomena in nanopores of various morphologies and topologies: testing the BET and BJH characterization methods. Particle & Particle Systems Characterization 21, 149–160.
Curtis, J.B., 2002. Fractured shale-gas systems. AAPG Bulletin 86, 1921–1938.
Curtis, M.E., Ambrose, R.J., Sondergeld, C.H., Rai, C.S., 2012. Microstructural investigation of gas shales in two and three dimensions using nanometer-scale resolution imaging. AAPG Bulletin 96, 665–677.
de Boer, J.H., Lippens, B.C., Linsen, B.G., Broekhoff, J.C.P., van den Heuvel, A., Osinga, Th.J., 1963. The t-curve of multimolecular N_2-adsorption. Journal of Colloid and Interface Science 21, 405–414.
Dombrowski, R.J., Hyduke, D.R., Lastoskie, C.M., 2000. Pore size analysis of activated carbons from argon and nitrogen porosimetry using Density Functional Theory. Langmuir 16, 5041–5050.
Groen, J.C., Peffer, L.A.A., Pérez-Ramírez, J., 2003. Pore size determination in modified micro- and mesoporous materials. Pitfalls and limitations in gas adsorption data analysis. Microporous and Mesoporous Materials 60, 1–17.
Hao, F., Zou, H., 2013. Cause of shale gas geochemical anomalies and mechanisms for gas enrichment and depletion in high-maturity shales. Marine and Petroleum Geology 44, 1–12.
Hill, R.J., Zhang, E., Katz, B.J., Tang, Y., 2007. Modeling of gas generation from the Barnett shale, Fort Worth Basin, Texas. AAPG Bulletin 91, 501–521.
Hodson, M.E., 1999. Micropore surface area variation with grain size in unweathered alkali feldspars: implications for surface roughness and dissolution studies. Geochimica et Cosmochimica Acta 62, 3429–3435.
Huang, J., Zou, C., Li, J., Dong, D., Wang, S., Wang, S., Cheng, K., 2012. Shale gas generation and potential of the Lower Cambrian Qiongzhusi Formation in the Southern Sichuan Basin, China. Petroleum Exploration and Development 39, 75–81.
Hunt, J.M., 1996. Petroleum Geochemistry and Geology, second ed. W. H. Freeman and Co., New York.
Jarvie, D.M., Hill, R.J., Ruble, T.E., Pollastro, R.M., 2007. Unconventional shale-gas systems: the Mississippian Barnett Shale of north-central Texas as one model for thermogenic shale-gas assessment. AAPG Bulletin 91, 475–499.
Krooss, B.M., Littke, R., Miiller, B., Frielingsdorf, J., Schwochau, K., Idiz, E.F., 1995. Generation of nitrogen and methane from sedimentary organic matter: implications on the dynamics of natural gas accumulations. Chemical Geology 126, 291–318.
Kuila, U., Prasad, M., 2013. Specific surface area and pore-size distribution in clays and shales. Geophysical Prospecting 61, 341–362.
Liang, C., Jiang, Z., Yang, Y., Wei, X., 2012. Shale lithofacies and reservoir space of the Wufeng–Longmaxi Formation, Sichuan Basin, China. Petroleum Exploration and Development 39, 736–743.
Long, P., Zhang, J., Jiang, W., Nie, H., Tang, X., Han, S., Xing, Y., 2012. Analysis on pores forming features and its influence factors of reservoir well Yuye-1. Journal of Central South University (Science and Technology) 43, 3954–3963.
Loucks, R.G., Reed, R.M., Ruppel, S.C., Jarvie, D.M., 2009. Morphology, genesis, and distribution of nanometer-scale pores in siliceous mudstones of the Mississippian Barnett Shale. Journal of Sedimentary Research 79, 848–861.
Loucks, R.G., Reed, R.M., Ruppel, S.C., Hammes, U., 2012. Spectrum of pore types and networks in mudrocks and a descriptive classification for matrix-related mudrock pores. AAPG Bulletin 96, 1071–1098.
Ma, Y., Feng, J., Mu, Z., Zhao, P., Bao, S., Wang, F., 2012. The potential and exploring progress of unconventional hydrocarbon resources in SINOPEC. Engineering Science 14, 2–29.
Magee, R.W., 1995. Evaluation of the external surface area of carbon black by nitrogen adsorption. Rubber Chemistry and Technology 68, 590–600.
Mahlstedt, N., Horsfield, B., 2012. Metagenetic methane generation in gas shales I. Screening protocols using immature samples. Marine and Petroleum Geology 31, 27–42.
Mastalerz, M., He, L., Melnichenko, Y.B., Rupp, J.A., 2012. Porosity of coal and Shale: insights from gas adsorption and SANS/USANS techniques. Energy & Fuels 26, 5109–5120.
Meyer, K., Klobes, P., 1999. Comparison between different presentations of pore size distribution in porous materials. Fresenius' Journal of Analytical Chemistry 363, 174–178.
Milliken, K.L., Rudnicki, M., Awwiller, D.N., Zhang, T., 2013. Organic matter–hosted pore system, Marcellus Formation (Devonian), Pennsylvania. AAPG Bulletin 97, 177–200.
Montgomery, S.L., Jarvie, D.M., Bowker, K.A., Pollastro, R.M., 2005. Mississippian Barnett Shale, Fort Worth Basin, north-central Texas: gas-shale play with multitrillion cubic foot potential. AAPG Bulletin 89, 155–175.
Nelson, P.H., 2009. Pore throat sizes in sandstones, tight sandstones, and shales. AAPG Bulletin 93, 1–13.
Pepper, A.S., Dodd, T.A., 1995. Simple kinetic models of petroleum formation. Part II: oil-gas cracking. Marine and Petroleum Geology 12, 321–340.
Pollastro, R.M., 2007. Total petroleum system assessment of undiscovered resources in the giant Barnett Shale continuous (unconventional) gas accumulation, Fort Worth Basin, Texas. AAPG Bulletin 91, 551–578.
Ross, D.J.K., Bustin, R.M., 2008. Characterizing the shale gas resource potential of Devonian-Mississippian strata in the Western Canada Sedimentary Basin: Application of an integrated formation evaluation. AAPG Bulletin 92, 87–125.
Ross, D.J.K., Bustin, R.M., 2009. The importance of shale composition and pore structure upon gas storage potential of shale gas reservoirs. Marine and Petroleum Geology 26, 916–927.
Rouquerol, J., Llewellyn, P., Rouquerol, F., 2007. Is the BET equation applicable to microporous adsorbents? Studies in Surface Science and Catalysis 160, 49–56.
Scherdel, C., Reichenauer, G., Wiener, M., 2010. Relationship between pore volumes and surface areas derived from the evaluation of N_2-sorption data by DR-, BET- and t-plot. Microporous and Mesoporous Materials 132, 572–575.
Schmitt, M., Fernandes, C.P., da Cunha Neto, J.A.B., Wolf, F.B., dos Santos, V.S.S., 2013. Characterization of pore systems in seal rocks using nitrogen gas adsorption combined with mercury injection capillary pressure techniques. Marine and Petroleum Geology 39, 138–149.
Schoenherr, J., Littke, R., Urai, J.L., Kukla, P.A., Rawahi, Z., 2007. Polyphase thermal evolution in the Infra-Cambrian Ara group (South Oman salt basin) as deduced by maturity of solid reservoir bitumen. Organic Geochemistry 38, 1293–1318.
Sing, K.S., Everett, D.H., Haul, R.A.W., Moscou, L., Pierotti, R.A., Rouquerol, J., Siemieniewsha, T., 1985. Reporting physisorption data for gas/solid systems with special reference to the determination of surface area and porosity. Pure and Applied Chemistry 57, 603–619.
Stach, E., Mackowsky, M.-T., Teichmüller, M., Taylor, G.H., Chandra, D., Teichmüller, R., 1982. Stach's Textbook of Coal Petrology. Gebrüder Borntraeger, Stuttgart.
Strąpoć, D., Mastalerz, M., Schimmelmann, A., Drobniak, A., Hasenmueller, N.R., 2010. Geochemical constraints on the origin and volume of gas in the New Albany Shale (Devonian–Mississippian), eastern Illinois Basin. AAPG Bulletin 94, 1713–1740.
Sun, W., Liu, S., Ran, B., Wang, S., Ye, Y., Luo, C., Tian, M., 2012. General situation and prospect evaluation of the shale gas in Niutitang Formation of Sichuan Basin and its surrounding areas. Journal of Chengdu University of Technology (Science & Technology Edition) 39, 170–175.
U. S. Energy Information Administration, 2011. World Shale Gas Resources: an Initial Assessment of 14 Regions Outside the United States.
Wang, L., Zou, C., Zheng, P., Chen, S., Zhang, Q., Xu, B., Li, H., 2009. Geochemical evidence of shale gas existed in the Lower Paleozoic Sichuan basin. Natural Gas Industry 29, 59–62.
Webb, P.A., Orr, C., 1997. Analytical Methods in Fine Particle Technology. Micromeritics, Norcross, GA.
Zeng, X.L., Liu, S.G., Huang, W.M., Zhang, C.J., 2012. Comparison of Silurian Longmaxi Formation shale of Sichuan Basin in China and Carboniferous Barnett Formation shale of Fort Worth Basin in United States. Geological Bulletin of China 30, 372–384.
Zhang, T.W., Ellis, G.S., Rupple, S.C., Milliken, K., Yang, R., 2012. Effect of organic-matter type and thermal maturity on methane adsorption in shale-gas systems. Organic Geochemistry 47, 120–131.
Zou, C., Dong, D., Wang, S., Li, J., Li, X., Wang, Y., Li, D., Cheng, K., 2010. Geological characteristics and resource potential of shale gas in China. Petroleum Exploration and Development 37, 641–653.